Journal of Colloid and Interface Science 708 (2026) 139781

Contents lists available at ScienceDirect

Journal of Colloid And Interface Science

journal homepage: www.elsevier.com/locate/jcis

A phase-field model: Contact angle hysteresis driven by multistable surface composition

Hongmin Zhang [a], Shan Lyu [b], Martin Reder [a,c,*], Nina Merkert [b], Britta Nestler [a,c,d]

[a] Institute of Nanotechnology, Karlsruhe Institute of Technology, Hermann-von-Helmholtz Pl. 1, 76344, Eggenstein-Leopoldshafen, Germany
[b] Institute of Metallurgy, Technical University of Clausthal, Adolph-Roemer-Straße 2A, 38678, Clausthal-Zellerfeld, Germany
[c] Institute of Applied Materials - Microstructure Modelling and Simulation (IAM-MMS), Karlsruhe Institute of Technology (KIT), Straße am Forum 7, 76131, Karlsruhe, Germany
[d] Institute of Digital Materials Science (IDM), Karlsruhe University of Applied Sciences, Moltkestraße 30, 76133, Karlsruhe, Germany

ARTICLE INFO

Keywords:
Contact angle hysteresis
Multistable surface compositions
Adsorption and depletion layers
Droplet friction

ABSTRACT

Experimental observations have revealed molecular-scale density depletion near hydrophobic substrates, suggesting a diffuse and structurally heterogeneous fluid-solid interface. Motivated by these findings, we hypothesise that the surface composition at the fluid-solid boundary may adopt multiple energetically favourable states. To account for this behaviour, we introduce a nonmonotonic wall free energy formulation that captures the energetic contribution of the fluid-solid interactions within the wetting boundary condition of a thermodynamically consistent phase-field model. This formulation successfully reproduces multistable surface compositions and enables the modelling of static contact angle hysteresis (CAH) on smooth, horizontally oriented substrates, arising from deposition histories. By allowing the wall free energy to relax and permit contact line motion via molecular diffusion, this model captures the dynamic CAH observed during droplet motion on inclined substrates. Unlike conventional phase-field CAH models, our framework requires no explicit input on contact-line velocity or prescribed contact angles and relies solely on thermodynamic energy minimisation; it automatically captures contact line pinning, as well as advancing and receding states. Upon droplet sliding with CAH, stick-slip behaviour naturally emerges. These findings demonstrate that both CAH and stick-slip behaviour can originate purely from molecular-scale fluid-solid interactions, underscoring the importance of surface composition and interfacial diffusion, factors often overlooked in classical hydrodynamic models. This framework provides a pathway to bridge thermodynamic and hydrodynamic perspectives, potentially enabling new insights into slip, friction, and no-slip behaviour at fluid-solid interfaces, with particular relevance for microfluidic applications.

1. Introduction

Contact angle hysteresis (CAH) is a universal wetting phenomenon central to advanced surface technologies, including self-cleaning, smart filtration, and bioadhesive and antifouling applications. A droplet resting on a horizontal substrate may exhibit a range of contact angles depending on how it is deposited. Tilting the substrate leads to an asymmetric deformation of the droplet's contact angles, yet the droplet often remains pinned. Sliding occurs only beyond a critical tilt, where the front and rear contact angles approach their static advancing (θ_A) and receding (θ_R) limits. The difference between these two limits defines CAH [1] and reflects a capillary imbalance that resists droplet motion, manifesting as drop friction [2]. Without CAH, even tiny perturbations would set droplets in motion. Understanding CAH is therefore crucial for applications in microfluidics, heat transfer, and surface engineering.

Despite extensive study, it still lacks a complete theoretical framework on CAH. Predicting water droplet motion on inclined surfaces remains challenging. Roughness and heterogeneity are traditionally regarded as the primary causes of CAH. Marmur's thermodynamic analysis [3] shows that such inhomogeneities create multiple local minima in surface free energy, leading to metastable states and hysteresis. Yet CAH also appears on smooth, chemically homogeneous solids [4,5] and even on liquid substrates [6], showing that surface inhomogeneity alone is insufficient to explain this phenomenon. Additional mechanisms have been proposed, including viscous dissipation [7], substrate deformation within the contact wedge, and molecular-scale fluid-solid interactions such as surface adaptation [8], contact line friction, and slide electrification [9]. These mechanisms and their role in drop friction are comprehensively reviewed by Butt et al. [2].

* Corresponding author.
E-mail addresses: hongmin.zhang@kit.edu (H. Zhang), martin_dominik.reder@h-ka.de (M. Reder).

https://doi.org/10.1016/j.jcis.2025.139781
Received 4 August 2025; Received in revised form 30 October 2025; Accepted 24 December 2025
Available online 31 December 2025

When the substrate is regarded as inert, the intermolecular attractive and repulsive forces experienced by fluid molecules at the fluid-solid interface differ from those within the bulk or at the fluid-fluid interface. Such disparities break interfacial symmetry and may induce molecular accumulation or depletion near the substrate. Consequently, the local fluid volume fraction at the substrate, termed surface composition, may deviate from its bulk value, leading to adsorption or depletion layers, a phenomenon known as surface composition effect. Experiments have revealed molecular-scale depletion layers characterised by diffuse and structured interfaces rather than atomically sharp boundaries [10,11]. These findings prompt two fundamental questions: (i) Is the surface composition inherently unique for a given material, or does the interface exhibit multistability in surface composition? (ii) If the latter holds, how does the multistable surface composition influence CAH and contact line dynamics? This study focuses on the latter question, seeking to elucidate how molecular-scale interfacial structures give rise to CAH and govern macroscopic droplet friction [12], a connection that remains poorly understood. To isolate this effect, we focus on flat, rigid, smooth, chemically homogeneous, and inert substrates with quasi-equilibrium droplets. In this regime, CAH arises solely from molecular-scale fluid-solid interactions, hereafter referred to as intrinsic CAH.

The coexistence of multistable surface compositions would directly challenge the classical assumption of a fixed fluid-solid interfacial tension [13]. Recent theoretical studies [14–16] suggest that the fluid-solid interfacial tension varies with surface composition. This variability introduces multiple local minima in the surface energy landscape, providing a natural mechanism for static CAH. However, these studies are formulated within a sharp-interface framework and inherently disregard the diffuse nature of interfacial structure and the associated composition gradients near the contact line. As a result, although they capture the role of surface composition in static CAH, their predictive power is limited: they fail to account for how surface composition profiles influence dynamic behaviours such as contact line motion, pinning-depinning, and frictional resistance on tilted ideal substrates, where partial contact line shifts often precede droplet sliding. A predictive framework that links surface composition to both static CAH and contact line dynamics remains elusive.

Conventional hydrodynamic models [17,18] treat the fluid as a structureless continuum and typically model CAH phenomenologically, by prescribing a fixed hysteresis window $[\theta_R, \theta_A]$ within which the contact line remains pinned. While practical, such models provide limited insight into the microscopic origin of CAH or the role of interfacial structure in contact line dynamics and friction. Molecular dynamics (MD) simulations [19] can capture intrinsic CAH but are limited by their small computational scale. A promising alternative is the phase-field model, a mesoscale approach that treats interfaces as diffuse and captures interfacial physics without ad hoc boundary conditions. This approach integrates seamlessly with hydrodynamic equations. As such, it is well suited for studying fluid-solid interactions in microfluidic systems. In phase-field wetting models, fluid-solid coupling is typically introduced via a surface-composition-dependent wall free energy [20–22], which shares density units with interfacial tension and quantifies the energetic cost of the substrate's presence. This term bridges molecular-scale fluid-solid interactions with macroscopic wetting behaviour. However, conventional phase-field models still struggle to reproduce intrinsic CAH, even in static cases on horizontal substrates. Most [23–25] continue to rely on prescribed strategies, similar to those used in hydrodynamic models. This limitation arises from the commonly adopted wall free energy, which typically yields a global minimum in the surface energy landscape. It results in a unique, energetically favoured surface composition and enforces a constant fluid-solid interfacial tension determined solely by the material system. As a result, it smears out the experimentally observed fluid-solid interfacial structures that may play a critical role in CAH and contact line dynamics.

In this work, we propose a physically grounded phase-field model that connects multistable surface composition to macroscopic wetting dynamics, a connection that, to the best of our knowledge, remains unexplored. The novelty of this model lies in incorporating multiple local minima into the wall free energy density to represent the diffuse interfacial structure near an ideal solid surface. Each minimum corresponds to a thermodynamically favourable surface composition. This formulation enables the emergence of metastable surface compositions that depend on wetting history. We examine two representative cases: (i) sessile droplets at equilibrium and (ii) droplets steadily sliding or sticking on inclined substrates. In both scenarios, the model captures intrinsic CAH without relying on artificial hysteresis windows, contact line velocities, or hydrodynamic inputs. It also reveals how multistable surface compositions naturally account for contact line dynamics, including pinning, depinning, and stick-slip motion. This thermodynamically consistent framework provides a basis for investigating fluid friction in microfluidic systems where wetting dominates transport behaviour, such as plasma clogging at Y-junctions in blood flow [26] or nanoparticle-based drug delivery [27].

2. Phase-field model

2.1. Governing equations

Considering a droplet resting on an ideal substrate surrounded by gas (Fig. 1(1, 2)), the total free energy of the system is formulated as

$$E = \int_\Omega \left[\frac{\gamma_{lg}}{\epsilon} \psi_b(\phi) + \epsilon \gamma_{lg} \|\nabla \phi\|^2 + f_g(\phi) + f_{vp}(\phi) \right] \mathrm{d}\Omega + \int_{\partial\Omega_w} f_{sr}(\phi_s)\, \mathrm{d}S, \tag{1}$$

where the first integral accounts for the energy between the immiscible liquid and gas phases within the fluid domain Ω, and the second describes the excess wall free energy of forming the fluid-solid interface at the substrate $\partial\Omega_w$. The phase-field order parameter $\phi \in [0, 1]$ denotes the local liquid volume fraction, with $\phi = 1$ for pure liquid, $\phi = 0$ for pure gas, and intermediate values within the diffuse interface. The composition ϕ_s denotes the order parameter on the substrate.

In Ω, the first term, $\frac{\gamma_{lg}}{\epsilon}\psi_b(\phi)$, adopts the dimensionless obstacle potential

$$\psi_b(\phi) = \begin{cases} \frac{16}{\pi^2}\phi(1-\phi) & \text{if } 0 \le \phi \le 1 \\ +\infty & \text{otherwise,} \end{cases} \tag{2}$$

which confines ϕ strictly to the physically meaningful range $[0, 1]$ by imposing an infinite energy barrier outside this interval. This potential has two minima at $\phi = 1$ and $\phi = 0$, representing the stable liquid and gas phases, respectively. The barrier between them penalises the presence of the liquid-gas interface, favouring a sharper phase separation. The second term, $\epsilon\gamma_{lg}\|\nabla\phi\|^2$, is the gradient energy density, which penalises spatial variations in ϕ and thus favours a smoother interface. The balance between these competing energies stabilises the diffuse liquid-gas interface and defines its excess free energy. Here, γ_{lg} is the liquid-gas interfacial tension and ϵ controls the width of the diffusive interface. Both are held constant in this work for a fixed material system. The third term, $f_g(\phi)$, accounts for the gravity effect when the droplet rests on an inclined substrate:

$$f_g(\phi) = \mathbf{g} \cdot \mathbf{z} \Big[\rho_l h(\phi) + \rho_g \big[1 - h(\phi)\big] \Big], \tag{3}$$

where $h(\phi) = \phi^3(6\phi^2 - 15\phi + 10)$ is an interpolation function, ρ_l and ρ_g are the densities of the liquid and gas phases, respectively, $\mathbf{g}$ is the gravity vector, and $\mathbf{z}$ is the position vector. The fourth term, $f_{vp}(\phi)$, enforces droplet volume conservation, leading to a volume-preserved Allen-Cahn-type phase-field model that improves computational efficiency. More discussions are shown in Refs. [22,28]. At $\partial\Omega_w$, the wall free energy density $f_{sr}(\phi_s)$ quantifies the short-range attractive and repulsive interactions between fluid and solid molecules, determined by

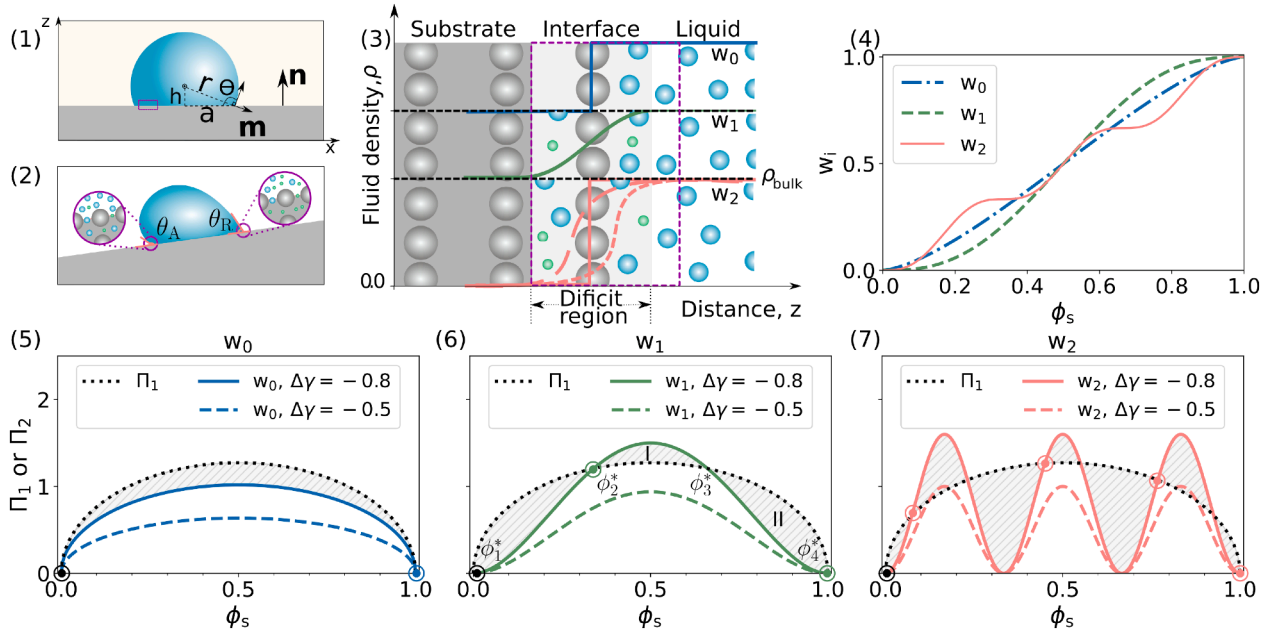

Fig. 1. **(1–2)** Schematic of a sessile droplet on horizontal and inclined solid surfaces. **(3)** Zoomed-in schematic of molecular arrangements at the liquid-solid interface: region (dark grey, bulk solid; light grey, interfacial zone); circles (grey, solid molecules; blue, liquid molecules; green, gas molecules). Three representative liquid density profiles are shown: blue, uniform profile with surface composition equal to bulk; green, monotonic transition to a single stable surface composition; pink, multiple density profiles, indicating multistable surface compositions. The final equilibrium surface composition is determined by the deposition history. **(4)** Wall free energy density functions w_0, w_1, and w_2 corresponding to these density profiles. **(5–7)** Analytical equilibrium surface compositions ϕ_i^* at $\Delta\gamma = -0.8$ and -0.5, obtained from Eq. (9). A less hydrophobic surface ($\Delta\gamma = -0.5$) weakens surface composition effects. (For interpretation of the references to colour in this figure legend, the reader is referred to the web version of this article.)

the local surface composition ϕ_s. This term is central to capturing intrinsic CAH in the present thermodynamic phase-field framework and is detailed later.

Focusing on the equilibrium state and steady droplet sliding, we neglect kinetic effects and apply an energy minimisation principle. Standard variational calculus on Eq. (1) gives the bulk and wall chemical potentials, μ_b and μ_s. Extending this framework to dynamics via the steepest descent method leads to the time-dependent evolution equation in the domain Ω:

$$-\mu_b = \tau_b \partial_t \phi = \gamma_{lg}\left[2\epsilon\nabla^2\phi - \frac{1}{\epsilon}\psi_b'(\phi)\right] - f_g'(\phi) - f_{vp}'(\phi), \tag{4}$$

subject to the wetting boundary condition (WBC) on $\partial\Omega_w$:

$$-\mu_s = \tau_s \partial_t \phi = 2\gamma_{lg}\epsilon\nabla\phi_s \cdot \mathbf{n} - f_{sr}'(\phi_s), \tag{5}$$

and the no-flux boundary condition on $\partial\Omega\backslash\partial\Omega_w$:

$$\nabla\phi_s \cdot \tilde{\mathbf{n}} = 0, . \tag{6}$$

Here, τ_b and τ_s are phenomenological relaxation parameters in the bulk and at the wall, respectively. The vector $\mathbf{n}$ is the unit normal to the substrate $\partial\Omega_w$, and $\tilde{\mathbf{n}}$ is the outward normal on the remaining boundaries $\partial\Omega \setminus \partial\Omega_w$, as shown in Fig. 1(1).

Simulations use a dimensionless water-air system based on three reference quantities: surface tension ($\sigma_{lg} = 72.8\,\mathrm{mN\,m^{-1}}$), characteristic length ($l_0 = 4\,\mu\mathrm{m}$), and characteristic time ($t_0 = 1\times10^{-4}\,\mathrm{s}$). Unless otherwise noted, all variables hereafter are presented in dimensionless form. Details of nondimensionalization, free energy formulation, and interface-width convergence are given in the Supplementary. It is essential to note that the present work focuses on the intrinsic CAH originating solely from wall free energy relaxation, thereby neglecting the effects of internal fluid dynamics. However, coupling the Navier-Stokes equations with phase-field models is possible using either a Cahn-Hilliard [29] or Allen-Cahn [30] type evolution equation and may be explored in future work.

2.2. Wall free energy formulations

Following the classical framework of Cahn [20], we define the short-range wall free energy density as:

$$f_{sr}(\phi_s) = \gamma_{ls} w(\phi_s) + \gamma_{gs}\left[1 - w(\phi_s)\right], \tag{7}$$

where γ_{ls} and γ_{gs} are the pure liquid-solid and gas-solid interfacial tensions. The wall free energy density function $w(\phi_s)$ satisfies $w(1) = 1$ and $w(0) = 0$, so that $f_{sr_0}(\phi_s = 1) = \gamma_{ls}$ and $f_{sr_0}(\phi_s = 0) = \gamma_{gs}$. Standard forms of $w(\phi_s)$, such as linear, polynomial, or sinusoidal profiles, are smooth and monotonic functions derived from ideal sub-regular solution theories based on van der Waals interactions [24]. Such profiles typically yield a global minimum, selecting a unique, energetically preferred surface composition. As such, these smooth formulations cannot reproduce surface composition multistability and thus fail to capture its role in intrinsic CAH within the traditional phase-field framework.

In adaptive wetting, even on ideal surfaces, interfacial structures can dynamically reorganise upon contact: fluid molecules may adsorb to or deplete from the solid surface, surface groups may reconstruct, diffusion and swelling can occur, and electric double layers may form, all strongly influenced by external perturbations [8]. These complex, coupled processes can give rise to nontrivial interfacial profiles, and thus to multistable surface compositions. Fig. 1(3) schematically illustrates molecular arrangements at the liquid-solid interface, along with three representative liquid density profiles reflecting varying degrees of adsorption or depletion. In the uniform case (w_0), the fluid density at the substrate equals the bulk value. In the monotonic case (w_1), the density deviates from the bulk but remains uniquely determined by the given material properties. In the nonmonotonic case (w_2), multiple metastable density profiles may coexist, with the equilibrium state determined by the deposition history. To represent these behaviours, we compare three wall free energy density functions, shown in Fig. 1(4), each corresponding to one of the density profile types:

$$w_0\text{: } w(\phi_s) = \frac{2}{\pi}\left[\arcsin(\sqrt{\phi_s}) + (2\phi_s - 1)\sqrt{\phi_s(1-\phi_s)}\right],$$

$$w_1\colon w(\phi_s) = \phi_s^3(6\phi_s^2 - 15\phi_s + 10),$$
$$w_2\colon w(\phi_s) = \phi_s - \frac{\sin(6\pi\phi_s)}{6\pi}. \tag{8}$$

Both w_0 and w_1 are smooth and monotonic, leading to a single energy minimum in $f_{sr}(\phi_s)$. In contrast, w_2 exhibits a smooth, but step-like, non-monotonic profile with multiple local extrema. This feature naturally introduces multiple metastable states into the system while maintaining thermodynamic consistency ($dE/dt \leq 0$) of the system.

3. Theoretical analysis

We show analytically, within the phase-field framework, that the existence of multiple stable surface compositions can give rise to intrinsic CAH. A brief outline is provided here; full derivations are documented in the Supplementary.

3.1. Surface composition effect

We first investigate the conditions under which the surface composition deviates from its bulk value, i.e., the surface composition effect, which leads to the formation of adsorption or depletion layers (hereafter referred to as wall layers) along the substrate. Under equilibrium and in one dimension, the natural WBC (Eq. (5)) reduces to:

$$\underbrace{\pm 2\gamma_{lg}\sqrt{\Delta\psi_b(\phi)}}_{:=\Pi_1} = \underbrace{\Delta\gamma\, w'(\phi_s)}_{:=\Pi_2}, \tag{9}$$

where the sign - corresponds to hydrophobic and + hydrophilic configurations, and $\Delta\psi_b(\phi) = \psi_b(\phi) - \psi_b(\phi_0) - (\phi - \phi_0)\psi_b'(\phi_0) = \psi_b(\phi)$. Here, $\phi_0 = 0$ represents the bulk gas phase. The interfacial energy difference, $\Delta\gamma = \gamma_{gs} - \gamma_{ls}$, quantifies the wall's relative affinity for gas and liquid: $\Delta\gamma > 0$ favors wetting (hydrophilic), $\Delta\gamma < 0$ favors dewetting (hydrophobic), and $\Delta\gamma = 0$ represents a neutral surface. A larger $|\Delta\gamma|$ indicates a stronger affinity contrast, making the surface more hydrophobic for negative $\Delta\gamma$ or more hydrophilic for positive $\Delta\gamma$.

Solving Eq. (9) yields a discrete set of admissible equilibrium surface compositions, $\mathcal{S} := \{\phi_i^* : i \in \mathbb{Z}^+\}$, from which the final equilibrium values beneath and outside the droplet, $\phi_{s_l}^*$ and $\phi_{s_g}^*$, are selected. Fig. 1(5–7) presents a graphical analysis of Eq. (9) for $\Delta\gamma = -0.8$ and -0.5, with black symbols denoting $\phi_{s_g}^*$ and colored symbols denoting $\phi_{s_l}^*$ for $\Delta\gamma = -0.8$. The results highlight that the surface composition effect depends primarily on two factors: (i) Wall free energy density formulation. The semi-obstacle form w_0 only yields trivial bulk-like solutions ($\phi_{s_g}^* = 0$ and $\phi_{s_l}^* = 1$), thereby suppressing surface composition effects and preventing wall layer formation. In contrast, both w_1 and w_2 permit ϕ_i^* to deviate from bulk values, allowing wall layers to form. (ii) Magnitude of $|\Delta\gamma|$. Increasing $|\Delta\gamma|$ (from -0.5 to -0.8) yields more $\Pi_1 - \Pi_2$ intersections for both w_1 and w_2. This implies that an increased interfacial energy difference strengthens surface composition effects and wall layering. As a result, within our framework, increasing surface hydrophobicity promotes multiple stable surface compositions, manifested as additional local minima in the surface free energy landscape (Supplementary fig. S1).

It is worth noting, however, that the presence of surface composition effects does not necessarily imply multiple stable surface compositions. At $\Delta\gamma = -0.8$, the smooth form w_1 yields four intersection points. The first, $\phi_1^* = 0$, corresponds to the equilibrium surface composition outside the droplet ($\phi_{s_g}^* = 0$). Beneath the droplet, the third intersection ϕ_3^* corresponds to a local maximum in surface energy, while ϕ_2^* and ϕ_4^* represent two local minima. The final $\phi_{s_l}^*$ is determined by a competition between the two minima, depending on the relative magnitudes of the integral areas I (increasing surface energy) and II (decreasing surface energy). At $\Delta\gamma = -0.8$, these areas are equal and thus both minima are equally stable, a critical wetting condition [20] that allows multistable surface composition. Away from this condition, the asymmetry in areas I and II favours a unique minimum. The step-like formulation w_2 exhibits up to eight intersections at $\Delta\gamma = -0.8$, four of which (colored symbols) correspond to local energy minima. The existence of multiple energy barriers between them necessitates that the determination of the final state $\phi_{s_l}^*$ must account for the dynamics of overcoming these barriers. This configuration supports robust multistability in surface composition, even away from the critical wetting condition, a necessary precursor for intrinsic CAH within the present framework.

3.2. Effective contact angle

We define a prescribed contact angle θ_p via $\cos\theta_p = \Delta\gamma/\gamma_{lg}$, where $\Delta\gamma = \gamma_{gs} - \gamma_{ls}$. Here, γ_{gs} and γ_{ls} are user-defined simulation parameters representing the fluid-solid interfacial tensions in the absence of surface composition effects. θ_p coincides with the classical Young's angle, as both assume constant interfacial tensions and neglect molecular variations at the fluid-solid interface. Intuitively, if the equilibrium surface composition $\phi_{s_g}^*$ or $\phi_{s_l}^*$ deviates from its bulk value, the effective interfacial tensions γ_{gs}^* and γ_{ls}^* are expected to differ from their nominal values γ_{gs} and γ_{ls}. Consequently, the effective contact angle θ^* may deviate from the prescribed angle θ_p.

To quantify this deviation, we integrate the natural WBC (Eq. (9)) from $\phi_{s_g}^*$ to $\phi_{s_l}^*$ across the liquid-gas interface on the substrate, yielding a modified Young's law:

$$\cos\theta^* = \frac{\gamma_{gs}^* - \gamma_{ls}^*}{\gamma_{lg}}, \tag{10}$$

with the effective interfacial tensions defined as:

$$\gamma_{gs}^* = f_{sr_0}(\phi_{s_g}^*) + 2\gamma_{lg}\int_{\phi_{s_g}^*}^{0}\sqrt{\Delta\psi_b(\phi)}\,d\phi,$$
$$\gamma_{ls}^* = f_{sr_0}(\phi_{s_l}^*) + 2\gamma_{lg}\int_{\phi_{s_l}^*}^{1}\sqrt{\Delta\psi_b(\phi)}\,d\phi. \tag{11}$$

This variationally derived θ^* is a microscopic contact angle that characterises the droplet profile around the contact line region, where the fluid-solid molecular interactions vary sharply [31]. In the present framework, these complex interactions are implicitly subsumed into γ_{gs}^* and γ_{ls}^*. Eq. (11) indicates that the effective fluid-solid interfacial free energy comprises two contributions: the wall free energy evaluated at the actual surface composition, and the excess free energy arising from the nonuniform composition profile within the wall layer.

In the absence of surface composition effects, i.e., $\phi_{s_g}^* = 0$ and $\phi_{s_l}^* = 1$, the integrals in Eq. (11) vanishes. Consequently, the effective interfacial tensions recover their prescribed values: $\gamma_{gs}^* = \gamma_{gs}$ and $\gamma_{ls}^* = \gamma_{ls}$, and the modified Young's law (Eq. (10)) reduces to the classical Young's law with $\theta^* = \theta_p$. However, when surface composition deviates from bulk values, $\theta^* \neq \theta_p$. If multiple stable surface compositions exist, as in the step-like form w_2, multiple values of θ^* can arise. This directly gives rise to intrinsic CAH, as demonstrated next through simulations.

4. Simulation results

4.1. CAH on horizontal substrates

Here, we examine a droplet resting on a horizontal substrate and compare theoretical predictions with numerical simulations for three wall free energy density formulations (w_0, w_1, and w_2), finding that the step-like $w_2(\phi)$ can reproduce deposition-history-dependent multistable surface compositions. This multiplicity thereby offers a promising thermodynamic route for reproducing intrinsic CAH on horizontal substrates.

Unlike the smooth formulation w_1, where the equilibrium surface composition follows a balance of integral areas, the outcome for w_2 also depends on the relaxation pathway because multiple energy barriers

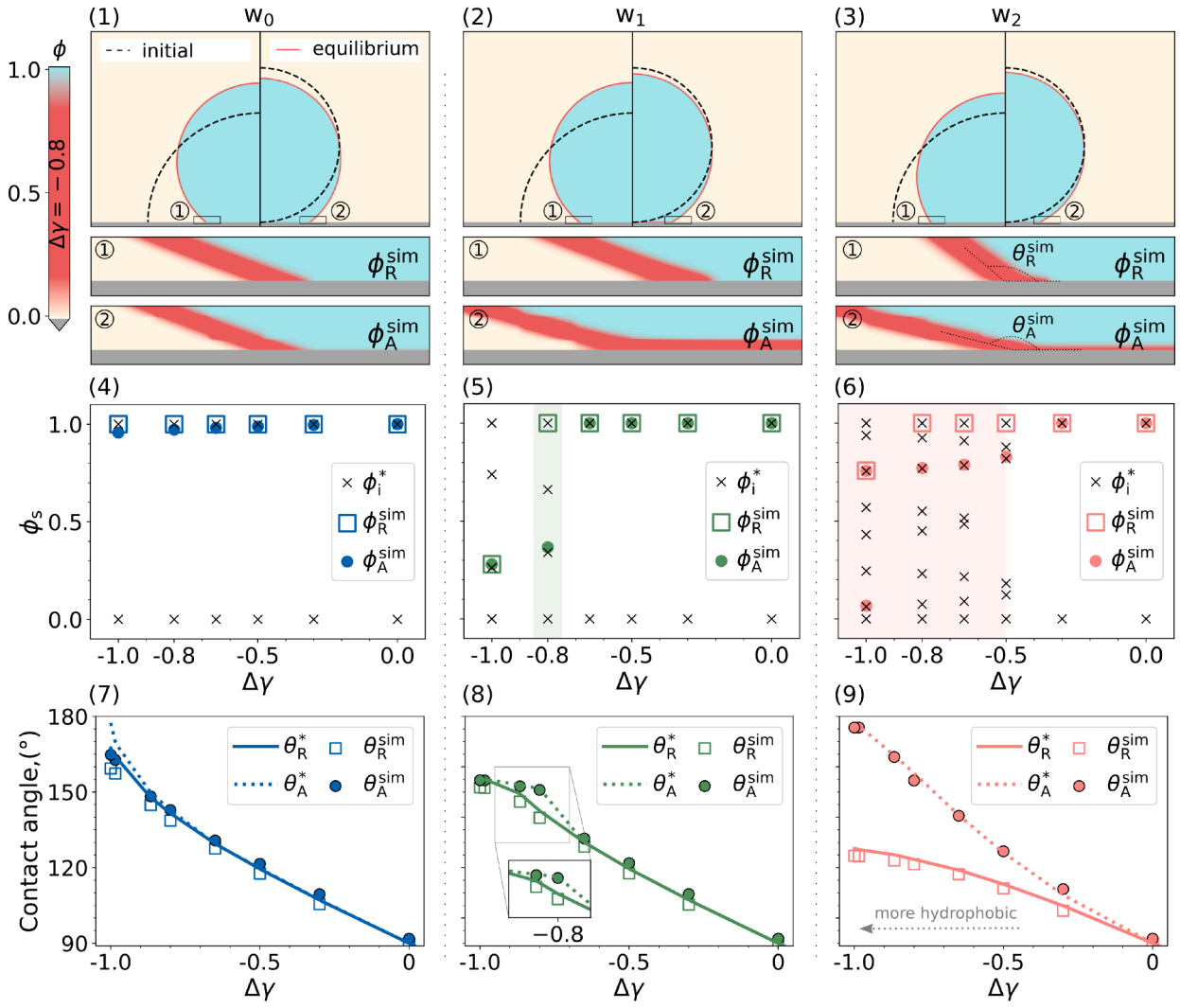

Fig. 2. **(1–3)** Simulation results for two distinct initial droplet shapes: *Left*: half-circle; *right*: full-circle. w_0: both cases converge to identical equilibrium states with no wall layer; w_1 and w_2: half-circle yields no wall layer, whereas full-circle forms a distinct wall layer, producing static CAH. **(4–6)** Quantitative comparison between theoretical and simulated equilibrium surface compositions across the full hydrophobic range. w_0: no multistable surface compositions; w_1: two multistable states only at $\Delta\gamma = -0.8$; w_2: pronounced multistability for $\Delta\gamma \leq -0.5$, giving rise to robust static CAH driven by deposition history. **(7–9)** Comparison of theoretical and simulated equilibrium contact angles as a function of the wettability parameter $\Delta\gamma$, for half-circle and full-circle initialisations. w_0: no measurable hysteresis across all $\Delta\gamma$, irrespective of initialisation; w_1: hysteresis appears only near the critical wetting condition ($\Delta\gamma = -0.8$); w_2: pronounced hysteresis is observed, confirming its capacity to capture intrinsic static CAH arising from different deposition histories.

exist. For instance, depending on initial conditions, the surface composition may evolve either from the bulk gas value (0) or the bulk liquid value (1) toward one of the stable states. To validate these predictions, we perform a series of two-dimensional simulations across the hydrophobic range ($\Delta\gamma \in [-1, 0]$), each initialised with either a half-circle (dewetting pathway) or a full-circle (wetting pathway) droplet to represent different deposition histories.

Fig. 2(1–3) illustrates simulation visualisations for three wall free energy density formulations at $\Delta\gamma = -0.8$. Black dashed lines mark the initial shapes; Insets ① and ② are enlarged for clarity. The colour bar represents the order parameter ϕ ranging from 0 to 1. For w_0, both initialisations yield nearly identical profiles, with the equilibrium surface compositions close to the bulk values, signifying the absence of wall layers. In contrast, w_1 and w_2 exhibit sensitivity to deposition history: pronounced wall layers form with full-circle initialisation but are absent in the half-circle case. Inset ① highlights a wedge-like intrusion for w_2, consistent with experimental reports of imperfect triple-junctions on superhydrophobic substrates [32]. In Inset ②, the wall layer in w_2 is visibly thinner than in w_1, reflecting weaker depletion. To understand this variation, we quantitatively analyse the surface composition in Fig. 2(4–6).

Theoretical values (ϕ_i^*, crosses) are compared with simulated equilibrium surface compositions across the full hydrophobic range. In this regime, the half-circle and full-circle initialisations produce distinct configurations which, if CAH exists, correspond to receding and advancing contact angles. Consequently, the equilibrium surface compositions beneath the droplet are denoted as ϕ_R^{sim} (squares) and ϕ_A^{sim} (circles), respectively, while the surface compositions outside the droplet, which naturally approach the bulk value (0), are therefore omitted. Fig. 2(7–9) further presents the corresponding contact angles as functions of $\Delta\gamma$: theoretical θ_R^* (solid) and θ_A^* (dotted) from the modified Young's law (Eq. (10)), alongside simulated θ_R^{sim} (squares) and θ_A^{sim} (circles). Across all three formulations, simulations agree well with theoretical predictions. The two panels quantitatively establish the link between deposition-history-dependent surface compositions and CAH.

For w_0, both initialisations relax to the same equilibrium ($\phi_R^{sim} \approx \phi_A^{sim} \approx 1$; $\theta_R^{sim} \approx \theta_A^{sim}$). This indicates a unique global minimum in the

surface free energy landscape (Supplementary fig. S1 (1)), eliminating multistability in surface composition and thus intrinsic CAH, irrespective of deposition history. Minor deviations reflect the inherent numerical limitations of the Allen-Cahn model [22].

For w_1, less hydrophobic substrates yield equilibrium surface compositions equal to the bulk liquid value (no wall layers). As $|\Delta\gamma|$ increases, surface composition effects emerge, accompanied by the formation of stable wall layers. These trends are consistent with experimental observations that increasing hydrophobicity enhances the stabilisation of depletion layers [11]. Deposition-history dependence ($\phi_R^{sim} \neq \phi_A^{sim}$) appears only near the critical wettability $\Delta\gamma \approx -0.8$, producing a finite hysteresis of $\Delta\theta^{sim} \approx 11°$. Outside this narrow window (green region in Fig. 2(5)), the imbalance between integral areas I and II favours a single energy minimum, yielding a unique equilibrium surface composition and no intrinsic CAH. Hence, w_1 produces static CAH only near critical wetting, contrary to numerous reports of static CAH on smooth substrates without such conditions [4,5], and therefore falls short in capturing the widely observed intrinsic CAH in real-world systems.

For w_2, multistable surface compositions and the associated intrinsic CAH robustly emerge across a broad hydrophobic range. When $\Delta\gamma \leq -0.5$, w_2 produces multiple local minima in the surface free energy landscape (Supplementary fig. S1 (3)), leading to deposition-history-dependent relaxation dynamics. Specifically, a half-circle droplet initialised with the liquid bulk composition beneath it (90°) undergoes dewetting, while a full-circle droplet initialised with the gas bulk composition (180°) follows a wetting path. These distinct relaxation routes converge to different energy minima characterised by distinct equilibrium surface compositions, i.e., $\phi_R^{sim} \neq \phi_A^{sim}$. Consequently, the resulting contact angles differ significantly, with $\theta_R^{sim} \neq \theta_A^{sim}$, and the hysteresis magnitude increases from approximately 11° at intermediate hydrophobicity to over 50° in the superhydrophobic regime. This hysteresis can be effectively tuned by adjusting the step-like profile of w_2. In contrast, for moderately hydrophobic surfaces ($\Delta\gamma > -0.3$), the surface free energy landscape flattens, and the multiple minima become less distinct or vanish entirely (Supplementary fig. S1 (3)). In this regime, distinct initial conditions relax to a single global minimum, yielding identical equilibrium states and eliminating hysteresis, consistent with a weakened depletion effect [11].

With surface composition effects, w_2 produces a higher surface composition than w_1 at the same $\Delta\gamma$. The resulting disparity between surface and bulk compositions establishes a diffuse wall layer, characterised by a gradual transition in composition normal to the substrate. Under identical wetting conditions, w_2 thus yields a narrower depletion zone than w_1, reflecting the influence of wall free energy formulation on the wall layer structure [33,34]. Variations in surface composition, induced by changes in wettability, temperature, or other factors, alter the surface-to-bulk transition and thereby the wall layer thickness. Explicitly, the wall layer thickness varies; implicitly, the effective solid-fluid interfacial tensions in Eq (11) are also affected. Through Eq. (10), these variations influence the final contact angle, consistent with experimental observations that interfacial tensions depend on the thickness of the wall layer [3].

At high hydrophobicity, particularly in the superhydrophobic regime, the surface composition profile from w_2 becomes highly nonuniform, featuring multiple depletion zones with distinct local values of ϕ_A^{sim}. This complexity necessitates numerical evaluation of the integrals in Eq. (11). Fig. 3 provides a zoomed view of the triple-junction region at $\Delta\gamma = -1.0$, revealing two zones with $\phi_A^{sim} = 0.75$ (box 1) and 0.07 (box 2); the latter reflects a pronounced depletion layer and a strongly inhomogeneous interfacial structure near the solid surface. These spatial variations align with high-resolution experimental observations of interfacial density fluctuations near the triple junction [10,11]. Such interfacial heterogeneity fundamentally challenges the measurements of the contact angle on superhydrophobic surfaces [35]. The microscopic contact angle θ^* is defined in a submicron region that is practically inaccessible to optical methods. Instead, experiments typically rely on goniometry, which estimates a macroscopic contact angle by extrapolating the droplet profile to a defined substrate baseline a (Fig. 1(1)). On superhydrophobic surfaces, however, this baseline becomes ambiguous: should it be placed at a_1, where the interface appears smooth and compositionally uniform, or at a_2, where the interface is strongly diffuse and depleted? Such ambiguity in baseline placement introduces substantial uncertainty in measured contact angles. As a result, contact angles reported on superhydrophobic surfaces often exhibit significant variability, in contrast to the relatively stable values observed for moderately wetting systems ($\theta \in [30°, 150°]$) [2]. To ensure consistency, all simulated contact angles in this work are calculated using the droplet's baseline a_1 and the droplet height h (Fig. 1(1)). Notably, although the theory in Eq. (10) predicts microscopic angles while simulations report macroscopic ones, observed agreement above is reasonable because droplets are small and the substrate is ideal.

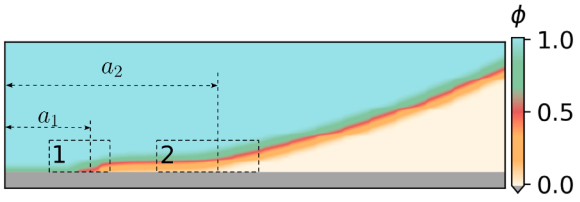

Fig. 3. Zoomed-in view of the triple junction for w_2 at superhydrophobicity ($\Delta\gamma = -1.0$), initialised with a full-circle droplet. The pronounced non-uniformity in surface composition yields distinct contact angle measurements at box 1 and box 2.

We further extend the systematic analysis across a broader wettability range ($\Delta\gamma \in [0, 1]$). On hydrophilic surfaces ($\Delta\gamma > 0$), the influence of initial conditions vanishes, as both droplet configurations follow the same wetting pathway and relax toward the same equilibrium state. The surface composition beneath the droplet (denoted as $\phi_{s_l}^{sim}$) converges to the bulk liquid value, while the composition outside the droplet ($\phi_{s_g}^{sim}$) approaches the bulk gas value, even in the superhydrophilic regime ($\theta < 30°$). In this regime, however, experimental observations show that the wetting wedge intrudes into the gas phase, causing $\phi_{s_g}^{sim}$ to exceed the bulk gas value and form an adsorption layer. Consequently, both initial conditions fail to form a stable wall layer in the fully hydrophilic regime, which prevents the emergence of intrinsic CAH (Supplementary fig. S2). This finding aligns with experimental reports that rarely detect static CAH on horizontally oriented hydrophilic substrates. To induce CAH on hydrophilic surfaces, external perturbations are typically required. In our context, tilting the substrate introduces gravity as an asymmetric perturbation between the front and rear contact lines. This asymmetry drives the formation of a wall layer near the triple line, thereby enabling the emergence of CAH even on hydrophilic surfaces.

4.2. CAH on inclined substrate

Here, we simulate droplet wetting on inclined substrates using three wall free energy density formulations, focusing on equilibrium or steady sliding states governed solely by thermodynamic energy minimisation. The results show that the step-like $w_2(\phi)$, owing to its nonmonotonic character, enables the model to naturally capture contact line pinning, advancing, and receding, thereby reproducing CAH under gravity. Once sliding begins, it further captures the characteristic stick-slip motion.

4.2.1. Droplet sliding criterion on inclined substrate

We place a droplet on a substrate inclined at $\alpha = 45°$ under gravity. The droplet begins to slide when the gravitational force component along the substrate exceeds the sliding resistance; otherwise, it remains pinned. Unlike classical solid-solid friction, which arises from interfacial roughness, droplet friction originates at the molecular level. Liquid molecules may become temporarily trapped in the solid lattice, forming a structure analogous to a molecular-scale Cassie-Wenzel state. In

the presence of CAH, earlier experiments [36] attribute this friction to an imbalance in capillary forces between the advancing and receding sides. This imbalance generates a net friction force, also called lateral adhesion force, defined as:

$$F_{la} = kl\gamma_{lg}(\cos\theta_R - \cos\theta_A), \tag{12}$$

where l is the effective footprint width and γ_{lg} is the liquid-gas surface tension. The geometric prefactor k accounts for the droplet deformation; we take $k = 1$ for 2D droplets. This formulation is primarily applicable to sessile or steady-state sliding droplets. In dynamic regimes, friction becomes velocity dependent and additional dissipation mechanisms (e.g., bulk and wedge viscous dissipation) must be considered [7].

The critical sliding condition is then determined by balancing the gravitational driving component and lateral adhesion force:

$$(\rho_l - \rho_g)Vg\sin\alpha = kl\gamma_{lg}(\cos\theta_R - \cos\theta_A), \tag{13}$$

where g is gravitational acceleration, and $V = 2\pi R_0^3/3$ is the droplet volume, initialised as a hemisphere with imaginary radius R_0 to ensure consistent volume across all cases. Introducing the Bond number, $\mathrm{Bo} = (\rho_l - \rho_g)gR_0^2/\gamma_{lg}$, which quantifies the ratio of gravitational to capillary forces, and approximating $l \approx 2R_0$, Eq. (13) reduces to a dimensionless sliding criterion [23]:

$$\mathrm{Bo}_c = \frac{\cos\theta_R - \cos\theta_A}{\frac{\pi}{3}\sin\alpha}, \tag{14}$$

which defines the critical Bond number separating pinned ($\mathrm{Bo} < \mathrm{Bo}_c$) and sliding ($\mathrm{Bo} > \mathrm{Bo}_c$) states. If $\mathrm{Bo} < \mathrm{Bo}_c$, the gravitational force is insufficient to overcome droplet friction, and the droplet remains pinned; otherwise, it slides.

Unlike conventional CAH models [25,37], which prescribe θ_A and θ_R as input parameters, our model incorporates energy barriers directly into the wall free energy. As a result, these angles emerge naturally from the simulations rather than being imposed a priori. Consequently, the values of θ_A and θ_R must be extracted from simulations. To investigate droplet sliding in the presence of CAH, we examine three representative surface wettabilities: $\Delta\gamma = -0.8$ (hydrophobic), 0.0 (neutral), and 0.8 (hydrophilic). For each case, the simulated advancing and receding contact angles (θ_A^{sim} and θ_R^{sim}) obtained in Section 4.1 are substituted into Eq. (14) to estimate the corresponding critical Bond number Bo_c.

For all three wettabilities considered with the w_0 and w_1 formulations, as well as for the natural surface case modelled with w_2, no stable CAH is observed on horizontal substrates, and the corresponding Bo_c is 0. This implies that even tiny perturbations are sufficient to initiate droplet motion. Interestingly, for the w_1 formulation at $\Delta\gamma = -0.8$, CAH does emerge under critical wetting conditions on a horizontal substrate. However, the droplet will slide freely on inclined substrates without exhibiting CAH, again yielding $\mathrm{Bo}_c = 0$, a point we elaborate on in the subsequent section.

In contrast, the w_2 formulation with $\Delta\gamma = -0.8$ exhibits clear CAH on horizontal substrates due to deposition history. Substituting the corresponding simulated contact angles into Eq. (14) yields a finite threshold of $\mathrm{Bo}_c \approx 0.52$. This value provides an order-of-magnitude estimate for the transition between pinned and sliding regimes. However, since the effective contact width l depends on droplet shape, and the advancing and receding contact angles vary with local wettability, a problem-dependent prefactor is required for quantitative estimation. For $\Delta\gamma = 0.8$, no CAH is observed on horizontal substrates using the w_2 formulation. Nevertheless, analysis of Eqs (10) and (11) suggests that CAH may develop under inclined conditions. Given that w_2 is symmetric with respect to $\pm\Delta\gamma$, we assume that the magnitude of CAH at $\Delta\gamma = 0.8$ is comparable to that at $\Delta\gamma = -0.8$, with an estimated $\mathrm{Bo}_c \approx 0.52$. To test this prediction, we perform simulations at two Bond numbers, Bo_1 and Bo_2, selected such that $\mathrm{Bo}_2 < \mathrm{Bo}_c = 0.52 < \mathrm{Bo}_1$. If CAH is present, as expected for the w_2 formulation at $\Delta\gamma = \pm 0.8$, the droplet is expected to remain pinned at Bo_2 and to slide at Bo_1.

4.2.2. 2D droplet wetting on inclined substrate

Fig. 4 shows 2D simulations of droplet wetting on an inclined substrate for the three wall free energy density formulations. Droplets are initially equilibrated without gravity. Upon activation of gravity at $t_0 = 0$ s, their motion is governed by CAH and gravity. To optimise space, the domains are displayed horizontally, with the substrate inclined at $\alpha = 45°$ and the gravity vector $\mathbf{g}$ indicated. The transformed domain size is with length L = 19.8 mm and height H = 3.6 mm.

Fig. 4(1) presents simulation snapshots for w_0 and w_1 at $\Delta\gamma = -0.8$, from t_0 to $t_3 = 0.048$ s. Both formulations yield identical sliding without CAH: droplets slide at both Bond numbers (Bo_1 and Bo_2) without deformation or interface asymmetry. At Bo_2, droplets move more slowly but still slide freely, showing no evidence of pinning. In both cases, the surface composition equals the bulk value, indicating no wall layer and no need to adjust fluid-solid interfacial tensions (Eq. (11)). The measured advancing and receding contact angles are identical $\theta_A = \theta_R \approx \theta_p$, recovering Young's law and agreeing with theoretical expectations. Similar behaviour is observed on hydrophilic and neutral surfaces; these cases are omitted for brevity.

Under horizontal conditions at $\Delta\gamma = -0.8$, the w_1 formulation yields distinct equilibrium surface compositions for two different initial states, resulting in a measurable static CAH. However, this hysteresis vanishes when the substrate is inclined. This behaviour can be interpreted from both dynamic and energetic perspectives. Dynamically, as discussed above, CAH is influenced by the relaxation dynamics of the wall free energy. This aligns with the mechanism proposed by Jacqmin [21] as well, in which such relaxation enables contact line motion via molecular diffusion. The monotonic profile of w_1 leads to equal driving forces at the front and rear contact lines, even under the influence of gravity, thereby suppressing droplet deformation and preventing the development of CAH. From an energetic standpoint, although the surface energy with w_1 has two local minima at $\Delta\gamma = -0.8$, this critical bistability is insufficient to maintain CAH under perturbations. On an inclined substrate, gravitational force acts asymmetrically on the droplet's leading and trailing edges, providing the perturbation needed to overcome the local energy barrier. Once this barrier is crossed, the system relaxes to the global minimum, yielding $\phi_{s_l}^{sim} = 1$ and $\phi_{s_g}^{sim} = 0$. This eliminates surface composition effects. As a result, no wall layer is sustained, and no CAH is observed on inclined substrates.

Fig. 4(2–4) present simulation snapshots for w_2 from t_0 to t_2, as the droplet on the hydrophilic surface at Bo_1 has already slid out the simulation domain by t_3. When $\Delta\gamma = 0$, surface compositions remain pinned to their bulk values (0 or 1), with no deviation observed either beneath or outside the droplet. Consequently, both droplets slide symmetrically without exhibiting contact angle asymmetry or deformation, demonstrating the same behaviour when using w_0 and w_1.

In contrast, for $\Delta\gamma = \pm 0.8$, significant surface composition effects arise on the inclined substrates, leading to the formation of a stable wall layer. On the hydrophilic surface, $\phi_{s_g}^{sim}$ stabilizes at 0.268, while on the hydrophobic surface, $\phi_{s_l}^{sim}$ equals 0.731. Notably, non-uniform distributions of surface compositions exist near the triple junction, as illustrated in Fig. 2(3). In the inclined configuration, asymmetric gravitational perturbations at the droplet's front and rear contact lines amplify this non-uniform distribution of surface composition near the triple junctions. These effects together induce asymmetric variations in the local fluid-solid interfacial tensions at the front and rear triple junctions, sustaining CAH even during droplet sliding.

As shown in Fig. 4(2) and (4), droplets with Bond number $\mathrm{Bo}_1 > \mathrm{Bo}_c$ begin to slide, while those with $\mathrm{Bo}_2 < \mathrm{Bo}_c$ remain pinned, consistent with our theoretical expectation. Droplet deformation arises as the advancing and receding contact angles diverge: on hydrophilic surfaces, the rear contact angle decreases, while on hydrophobic surfaces, the front contact angle increases. These asymmetric responses reflect the presence of CAH under inclination and confirm that the nonmonotonic nature of w_2 is sufficient to sustain hysteresis in droplet motion.

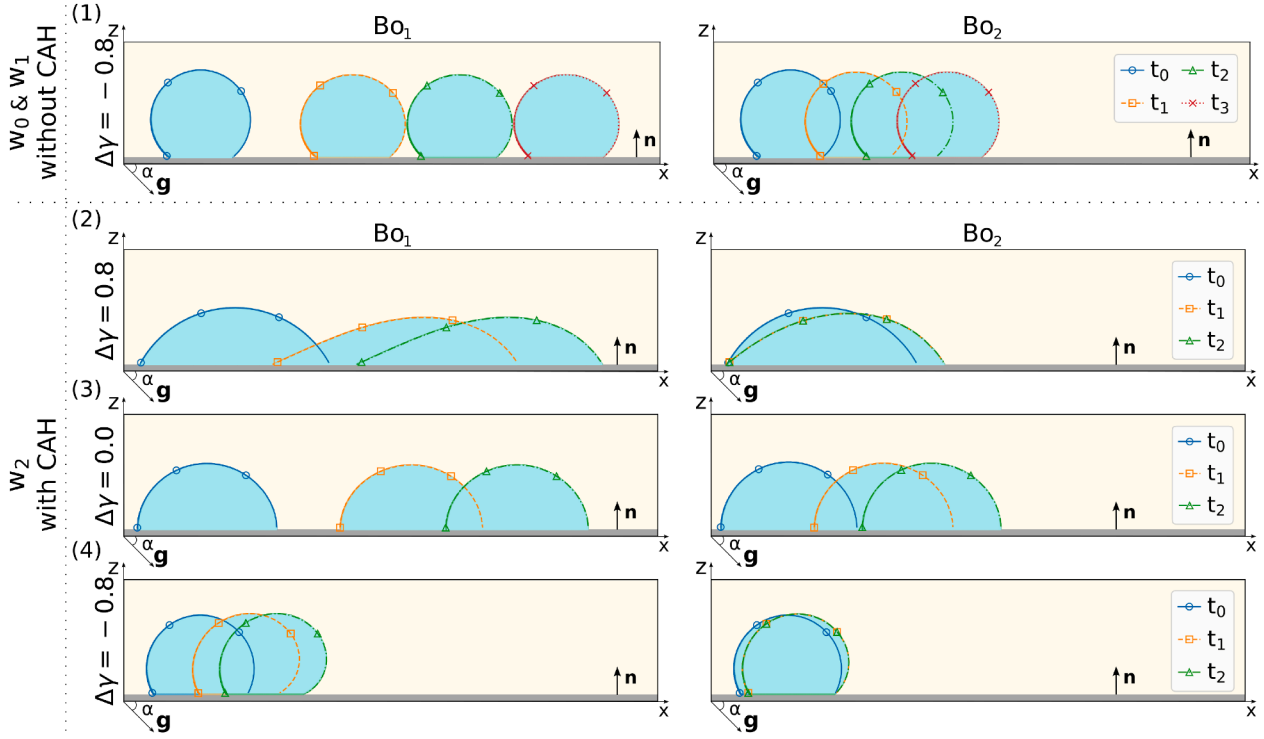

Fig. 4. Simulation snapshots of droplets on inclined substrates at $t_0 = 0$ s, $t_1 = 0.02$ s, $t_2 = 0.034$ s, and $t_3 = 0.048$ s ($\alpha = 45°$, **g** indicates gravity). **(1)** w_0 and w_1: no CAH; droplets slide symmetrically at both Bond numbers, with Bo_2 sliding more slowly than Bo_1. **(2–4)** w_2 captures contact line pinning as well as advancing and receding, thereby reproducing CAH. At $\Delta\gamma = 0$, the absence of multistable surface compositions yields symmetric, unimpeded sliding for both Bond numbers. At $\Delta\gamma = \pm 0.8$, CAH emerges, sliding at Bo_1 and pinning at Bo_2. This behaviour is accompanied by pronounced front-rear asymmetry, with a decreasing receding angle on hydrophilic surfaces and an increasing advancing angle on hydrophobic surfaces.

In the sliding case ($Bo_1 > Bo_c$), the droplet shape reaches a quasi-steady state between t_1 and t_2, with θ_A and θ_R unchanged. For $\Delta\gamma = 0.8$, it travels approximately 0.18 L along the substrate (with footprint length of ~ 0.37 L), corresponding to an average sliding velocity of $v \approx 0.25\ \mathrm{m\,s^{-1}}$, in good agreement with the experimentally measured values by Li *et al.* [7]. On the hydrophobic surface ($\Delta\gamma = -0.8$), the droplet displacement is only 0.04 L over the same time interval (footprint length $\sim$ 0.12 L), yielding a lower velocity of $v \approx 0.057\ \mathrm{m\,s^{-1}}$. It is important to emphasise that these simulations are conducted within a purely energy minimisation framework without hydrodynamic coupling. In this context, contact line motion is governed entirely by molecular diffusion, driven by the relaxation of the wall free energy, rather than by fluid flow. As a result, droplets on hydrophilic surfaces tend to elongate and exhibit faster sliding velocities compared to those on hydrophobic surfaces. This behaviour does not contradict experimental findings, where droplets typically move faster on hydrophobic surfaces due to additional mechanisms such as slip, rolling, or tank-treading mechanisms. For instance, in high capillary number regimes [7] or the presence of nanostructured coatings [38], fluid motion can be dominated by rolling or tank-treading mechanisms, neither of which is captured in the present framework. This work focuses on demonstrating CAH arising solely from fluid-solid interactions that induce multistable surface compositions. The interplay with hydrodynamic mechanisms in droplet motion will be explored in future studies.

For the stick case with $Bo_2 < Bo_c$, droplets on both hydrophilic and hydrophobic surfaces remain pinned on the inclined substrate. While comparing the buildup of CAH from the initial shape at t_0 to the near-equilibrium configuration at t_1, distinct wetting behaviours are observed depending on the surface character. On the hydrophilic surface, the rear contact line remains pinned while the receding contact angle decreases. In contrast, the advancing contact angle remains nearly unchanged, with the front contact line gradually advancing to adjust the droplet shape and enable relaxation toward a local energy minimum. This asymmetry in contact line dynamics is consistent with the CAH development mechanism reported by Yue [23]. On the hydrophobic surface, an opposite trend is observed: the front contact line remains pinned while the rear contact line retracts. This behaviour is accompanied by an increase in the advancing contact angle and a relatively constant receding angle, indicating a contrasting mode of CAH buildup.

4.2.3. *Mechanismus of droplet stick-slip sliding*

To further characterise droplet sliding behaviour under inclination, Fig. 5 extracts the time evolution of advancing and receding contact angles (θ_A and θ_R), along with the corresponding sliding friction force, for the step-like wall free energy density formulation w_2. The top panel shows the temporal evolution of the lateral adhesion force F_{la} (left y-axis), plotted as solid and dotted lines for Bo_1 and Bo_2, respectively. This force is calculated by substituting the simulated 2D contact length as l into Eq. (12). The corresponding advancing and receding contact angles are shown on the right y-axis: filled and open circles represent Bo_1, while filled and open squares correspond to Bo_2. The x-axis indicates simulation time steps; representative droplet shapes at t_0, t_1, and t_2 are shown in Fig. 4.

In the neutral case ($\Delta\gamma = 0.0$), both θ_A and θ_R remain fixed at 90°, and F_{la} is negligible throughout the simulation. The droplet maintains symmetric motion without deformation and exhibits smooth flow without stick-slip behaviour.

In contrast, for $\Delta\gamma = \pm 0.8$, gravity induces droplet deformation from t_0, causing the divergence between θ_A and θ_R and leading to a buildup in lateral adhesion force. For Bo_1, two distinct regimes emerge: a static regime (purple background in Fig. 5) where the droplet deforms but remains pinned, and a kinetic regime (orange background) where sliding occurs. This qualitative behaviour agrees well with experimental observations by Gao et al. [39].

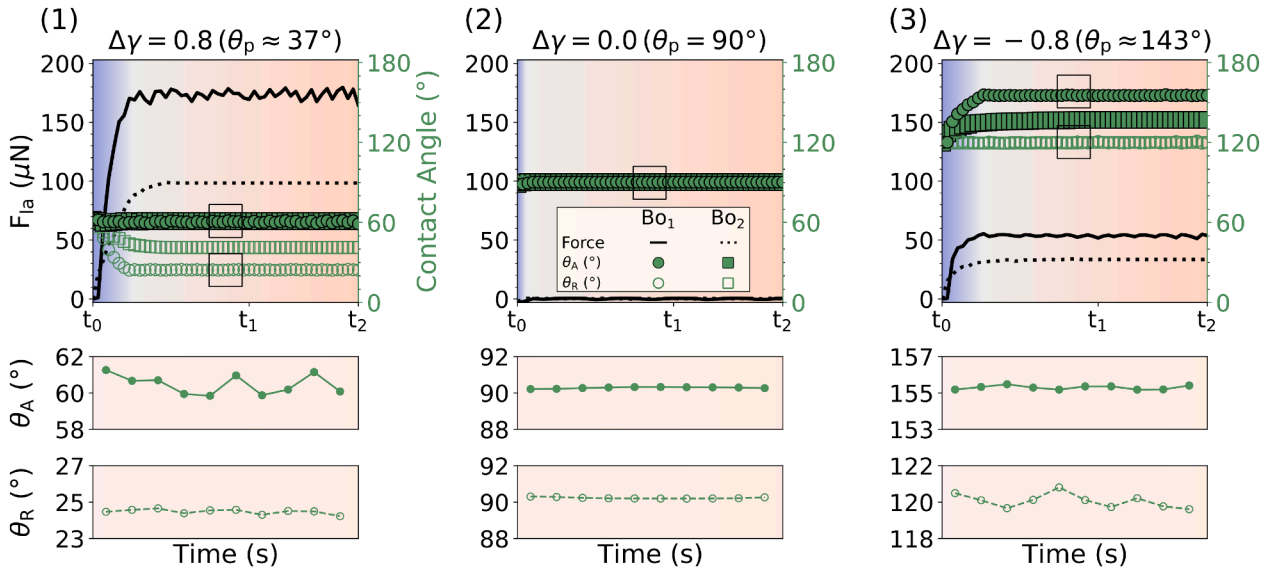

Fig. 5. Time evolution of lateral adhesion force and advancing & receding contact angles for the step-like w_2. Middle and bottom panels: zoomed-in views for the sliding case (Bo_1) showing stick-slip dynamics. At $\Delta\gamma = 0$, no CAH occurs and sliding is smooth. At $\Delta\gamma = \pm 0.8$, CAH appears; once sliding begins, sawtooth-like oscillations in F_{la} arise from contact angle fluctuations, indicating diffusion-driven stick-slip motion near the contact lines. The mechanism observed here is sustained by fluctuations of previously unchanged contact angles in the static region (highlighted by purple), θ_A on hydrophilic surfaces and θ_R on hydrophobic surfaces. (For interpretation of the references to colour in this figure legend, the reader is referred to the web version of this article.)

On the hydrophilic surface, for Bo_2, θ_R decreases from 62° to 41° while θ_A remains constant. This asymmetry leads to a rise in F_{la} until it balances the gravitational component along the incline. The droplet remains pinned in this state, and the contact angle difference saturates at approximately $\Delta\theta^{sim} \approx 21°$. For the higher Bond number Bo_1, θ_R decreases further to 24°, eventually triggering droplet sliding. On the hydrophobic surface, a contrasting mechanism is observed: θ_R remains unchanged, while θ_A increases from 120° to 137° for Bo_2, where the lateral adhesion force balances gravity. For Bo_1, θ_A reaches 155°, with a maximum angle difference of $\Delta\theta^{sim} \approx 35°$, marking the threshold for sliding onset. Notably, the measured advancing and receding contact angles deviate by less than 2° from θ_A^{sim} and θ_R^{sim}, respectively, as defined in Section 4.1. This confirms our expectation that the full-circle and half-circle initialisations recover the advancing and receding contact angles under CAH on a horizontal substrate. Moreover, the advancing-receding angle differences for $\Delta\gamma = \pm 0.8$ are nearly identical under both Bond number conditions. Together, these observations support the validity of our earlier hypothesis for determining the critical Bond number, as formulated in Eq. (14). The contrasting CAH buildup mechanisms observed for $\Delta\gamma = \pm 0.8$ suggest that the advancing and receding behaviours are governed not solely by spatial orientation, but also by the kinetic response relative to the initial configuration, aligning with the argument by Gao et al. [40]. Finally, the measured critical lateral adhesion force F_{la} is significantly lower on the hydrophobic surface (approximately 50 μN) than on the hydrophilic one (approximately 150 μN), consistent with experimental results [39].

In the Bo_1 cases, once droplet motion begins on both hydrophilic and hydrophobic surfaces, the system reaches a quasi-steady sliding state. This behaviour aligns with our assumption that, in the absence of external dissipation mechanisms, such as macroscopic roughness or viscous drag, the droplet slides steadily. However, small sawtooth-like oscillations in F_{la} appear within the kinetic regime. These fluctuations arise from the detailed dynamics of contact line motion. A zoomed-in view of the advancing and receding contact angles is shown in the middle and bottom panels of Fig. 5, respectively. During sliding, contact angles that were previously constant in static regions begin to fluctuate mildly within a hysteresis window. On the hydrophilic surface, the advancing angle varies between approximately 60° and 62°, while the receding angle remains pinned near 24°; on the hydrophobic surface, the advancing contact angle stays pinned, while the receding angle fluctuates slightly within the range [119°, 121°]. These angle variations reflect the alternation of lateral adhesion forces, acting as pinning or depinning forces, to balance the gravity component. The alternation is indicative of recurrent contact line depinning and repinning, resulting in a stick-slip droplet motion. In our model, this stick-slip behaviour arises solely from diffusion dynamics near the contact region. As previously discussed, on the hydrophilic surfaces, diffusion may dominate the contact line motion, whereas on hydrophobic surfaces, other mechanisms may play a more significant role. This interpretation is supported by experimental observations from Mirsaidov et al. [41], who reported that nanodroplets on a hydrophilic surface advance through a series of stick-slip steps rather than smooth flow. We propose that such stick-slip dynamics may be diffusion-driven in the absence of flow, although further quantitative investigation is necessary. In particular, whether the buildup of stick-slip motion driven by small fluctuations in the unchanged contact angles in the static region is a general phenomenon remains an open question, requiring higher-resolution measurements or advanced molecular dynamics simulations.

Last but not least, the stick-slip dynamics in our simulations arise purely from the relaxation of wall free energy within the diffusive interface framework. Unlike experimental systems, our model neglects macroscopic surface roughness, viscous dissipation, and slip at the solid-liquid interface. Consequently, the lateral adhesion force in our simulations does not exhibit an evident decay, as observed in experiments, where the force typically drops sharply and then reaches a plateau following droplet slip. Gao et al. [39] demonstrated that this post-slip force reduction strongly depends on the macroscopic roughness of the substrate. For instance, the decrease in lateral adhesion force for droplets on smooth silicone substrates is approximately 10 %, significantly less than that observed on rougher surfaces coated with silicone nanofilaments, titanium dioxide nanoparticles, or crosslinked polydimethylsiloxane. These surface structures promote partial liquid entrapment within asperities, forming a mixed Cassie-Wenzel wetting state that behaves like a virtual spring, modulating the effective contact area and storing interfacial energy. Such mechanisms alter the activation energy required for droplet motion compared to that on mechanically smooth

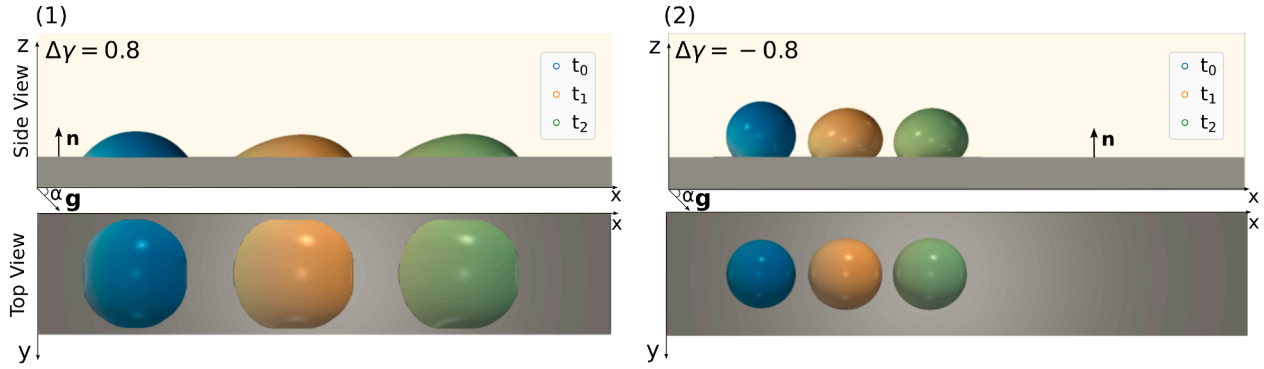

Fig. 6. 3D simulation snapshots of droplets on inclined substrates at Bo_1 using w_2: t_0 (blue), t_1 (orange), and t_2 (green). In both cases, droplets slide steadily. On the hydrophilic surface, the footprint elongates into two semicircles joined by straight sides parallel to the motion, consistent with theory and experiments. (For interpretation of the references to colour in this figure legend, the reader is referred to the web version of this article.)

Table 1
Comparison of CAH models: literature vs. present work.

Models	Origin of CAH	Static CAH on smooth substrate	CAH on inclined substrate	Stick-slip sliding	Hydrodynamic coupling	Notes
Spelt (2005) [37]	Prescribed	Not captured	Captured	Not captured	Optional	Empirically prescribed hysteresis window
Yue (2020) [23]	Prescribed	Not captured	Captured	Not captured	Yes	Hysteresis window incorporated into wall free energy relaxation
Wang *et al.* (2024) [14,16]	Multistable surface composition	Captured	Not captured	Not captured	No	Theoretical framework
Present work	Multistable surface composition	**Captured**	**Captured**	**Captured**	Framework ready	Physically grounded mesoscale model for fluid-solid interactions; requiring no geometric input

substrates. Further investigation into the roles of macroscopic roughness and internal fluid flow during droplet motion is warranted in future work.

4.2.4. 3D droplet sliding with CAH

We further perform 3D simulations of droplets sliding on inclined hydrophilic and hydrophobic substrates using the w_2 formulation. Fig. 6 presents the side and top views for the Bo_1 configuration. For space considerations, pinned cases at Bo_2 are provided in the Supplementary.

As shown in the side view of Fig. 6, both cases exhibit clear CAH, with distinct advancing and receding contact angles. The top view reveals that the simulated footprint of the hydrophilic droplet agrees well with theoretical predictions [36]: which, when the droplet slides in steady state, the footprint is elongate and approximated by two semicircles joined by straight sides parallel to the direction of motion. In contrast, the droplet on the hydrophobic surface displays much less pronounced elongation. This observation is consistent with experimental findings by Extrand et al. [42], which show that the footprint aspect ratio (length to width) increases with the hysteresis ratio, defined as $\mathcal{R} = \Delta\theta/\theta_A$. In our simulations, the hydrophilic case ($\mathcal{R} = 0.34$) exhibits greater elongation than the hydrophobic case ($\mathcal{R} = 0.22$), in agreement with this trend. To fully capture the front-rear asymmetry in droplet shape during sliding, the internal fluid flow within the droplet should be incorporated into our future model.

5. Discussion

This section addresses the physical plausibility and implications of the proposed step-like wall free energy density formulation concerning fluid-solid interactions in microfluidic simulations.

5.1. Physical plausibility of the step-like form w_2

The proposed step-like wall free energy density, w_2, permits the existence of multistable surface compositions. This feature allows the phase-field model to account for intrinsic CAH, driven by deposition history, as well as contact line dynamics such as pinning, advancing, and receding. Here, we assess the physical plausibility of this formulation by considering: (i) the thermodynamic feasibility of multiple energetically favourable surface compositions coexisting at the fluid-solid interface; (ii) the emergence of corresponding local minima in the wall free energy landscape, which provide the necessary conditions for CAH.

Conventional wall free energy density functions in phase-field models [21,22] are derived from regular solution theory, which assumes a unique surface composition beneath and outside the droplet. This yields a surface free energy landscape with a single global minimum, thereby precluding the emergence of CAH from a thermodynamic perspective. This stands in contrast to experimental evidence showing multiple local minima in surface free energy when CAH is present [43,44]. Moreover, smooth wall free energy density formulations oversimplify interfacial physics by neglecting the structural asymmetry between mobile fluid molecules and immobile solid atoms. Near the solid surface, fluid molecules experience distinct constraints compared to those in the bulk, giving rise to interfacial behaviours not captured by conventional formulations.

Experimental evidence further underscores the structural complexity of fluid-solid interfaces. On superhydrophobic surfaces, the water density near the solid wall exhibits nanoscale inhomogeneities within a molecular-scale depletion layer [10,11]. In polymer systems, analogous interfacial depletion can extend up to micrometers [45] and may exhibit pronounced near-wall density fluctuations. Additionally, Tadmor et al. [46] observed increased adhesion with contact time, attributed to the formation and rupture of transient molecular bonds. This behaviour can be rationalised with a spring model in which longer contact durations strengthen interfacial bonding and raise frictional resistance. Such observation supports viewing CAH as a thermally activated process involving molecular hopping among metastable states. Together, these findings suggest the plausible coexistence of multiple metastable surface compositions, as illustrated schematically in Fig. 1(3). However,

phase-field models employing smooth wall free energy density formulations impose a single equilibrium surface composition and enforce homogeneous composition profiles, inherently smoothing out the interfacial fluctuations and limiting their ability to capture intrinsic CAH.

Wang et al. [14], working within the framework of multistable surface compositions, theoretically demonstrated how liquid-gas density asymmetry, fluid-solid van der Waals interactions, and intermolecular potentials collectively determine the final surface composition and, consequently, the effective composition-dependent interfacial energy. This competition yields multiple minima in the surface energy landscape, offering a microscopic basis for intrinsic CAH on nominally smooth substrates. Building on the same framework, Wang et al. [16] incorporated the disjoining pressure into the composition-dependent wall free energy. By linking pressure to composition via Dalton's law and applying the Young-Laplace equation, they introduced the effect of gravity into fluid-solid interfacial energy. This concept quantifies the gravity-induced contribution to line tension and explains its sign and magnitude, resolving longstanding inconsistencies among experimental measurements. Together, their findings reinforce the surface composition effect as a unifying framework for interpreting wetting phenomena by accounting for composition-dependent interfacial energies. Their analysis offers key insights into the origin of CAH and supports the view that surface composition is not necessarily unique or constant, but multistable, state-dependent, and responsive to molecular-scale structure.

To directly illustrate the impact of surface composition on wetting behaviour, we performed MD simulations as quantitative support for our argument: surface composition might vary spatially rather than always being a unique value. An aluminium (Al) droplet is placed on the single-crystal copper (Cu) substrate, which has three crystallographic orientations: (001), (110), and (111). Near equilibrium, Al droplet on Cu (001) and Cu (110) exhibits similar wetting behaviour: only limited diffusion occurs at the liquid-solid interface. An atomic-thick precursor film is clearly visible on both substrates. This layer leads to a local density overshoot, which then decays and settles to the bulk density. In contrast, on the Cu (111) substrate, significant dissolution occurs across the interface, which results in a lower Al density compared to the bulk density; Cu atoms cross the interface and continue diffusing deep into the droplet interior, producing a diffuse interfacial zone. The differing equilibrium contact angles on the three substrates ($\theta = 29°$ on Cu (001), 28° on Cu (110), and 18° on Cu (111)) indicate that the liquid-solid interfacial tension is sensitive to local molecular interactions and varies with surface compositions. Simulation details are provided in the Supplementary.

In general, surface composition at fluid-solid interfaces is influenced by a variety of factors, including but not limited to molecular polarity, surface charge, particle size, and interfacial alignment of polar groups. These factors collectively shape a rugged energy landscape with multiple metastable states. Building on these insights, our step-like wall free energy density formulation extends the smooth sinusoidal forms [37] by introducing multiple local minima. These minima mimic physical perturbations caused by multibody interactions at the fluid-solid interface. Although difficult to model explicitly, such interactions reflect realistic interfacial complexity and justify the existence of multiple stable states within the diffuse interface. This, in turn, enables the phase-field model to support distinct advancing and receding contact angles.

5.2. Outlook for fluid-solid interface

Finally, we emphasise the broader implications of the proposed step-like wall free energy density formulation beyond CAH studies. Traditional hydrodynamic models typically impose slip or no-slip conditions without explicitly accounting for molecular interactions at the fluid-solid interface. While bridging microscopic diffusion and macroscopic flow is a promising idea, slip emerges naturally from interfacial molecular interactions rather than being prescribed. Recent theoretical advances [47] support this perspective through the introduction of a wall layer.

Our step-like wall free energy density formulation enables the phase-field model to numerically implement such a wall layer by directly encoding molecular-scale interactions, thereby capturing CAH without relying on imposed hydrodynamic boundary conditions. This highlights the critical role of interfacial structure in determining CAH, an aspect often overlooked in experiments and conventional hydrodynamic models of wetting. This framework lays a foundation for future microfluidic simulations that couple hydrodynamic and thermodynamic effects. In the context of droplet motion, the wall layer facilitates a quantitative exploration of frictional dissipation and the interplay between slip, no-slip, and diffusion-driven contact line motion, which are crucial for optimising droplet transport and surface functionality.

6. Conclusion

This work develops a physically grounded, thermodynamically consistent phase-field model in which contact angle hysteresis (CAH) emerges directly from molecular-scale fluid-solid interactions. Motivated by experimental evidence of depletion and adsorption layers [10,11], we assume the existence of multistable surface compositions [14,15] at the fluid-solid interface and propose a step-like, non-monotonic wall free energy density. Unlike the conventional smooth form [22], which leads to a unique equilibrium surface composition, our formulation naturally produces metastable surface states. As shown in Table 1, this approach reproduces:

- static CAH on smooth substrates arising from different deposition processes;
- CAH on inclined substrates, naturally capturing contact line pinning as well as advancing and receding states;
- intrinsic stick-slip sliding.

These behaviours arise without imposing a hysteresis window [23,37], specifying geometric details, or coupling to hydrodynamics, revealing that both CAH and stick-slip sliding can originate purely from interfacial molecular physics.

This work highlights the importance of fluid-solid interactions and offers a robust framework for coupling these interactions with continuum hydrodynamics. It opens the door to new frontiers in quantitatively exploring viscous-frictional dissipation and the dynamic interplay of slip, no-slip, and diffusion-driven motion, paving the way for innovations in microfluidics and droplet-based technologies.

Declaration of Generative AI and AI-assisted Technologies in the Writing Process

During the preparation of this work, the authors used ChatGPT in order to improve language and readability. After using this tool, the authors reviewed and edited the content as needed and take full responsibility for the content of the publication.

CRediT authorship contribution statement

Hongmin Zhang: Writing – original draft, Visualization, Validation, Methodology, Investigation, Formal analysis, Data curation, Conceptualization; **Shan Lyu:** Writing – review & editing, Visualization, Validation, Methodology, Investigation; **Martin Reder:** Writing – review & editing, Supervision; **Nina Merkert:** Writing – review & editing, Funding acquisition; **Britta Nestler:** Writing – review & editing, Project administration, Funding acquisition.

Data availability

Data will be made available on request.

Declaration of competing interest

The authors declare that they have no known competing financial interests or personal relationships that could have appeared to influence the work reported in this paper.

Acknowledgments

This research is supported by the Gottfried-Wilhelm Leibniz prize NE 822/31-1 of the German Research Foundation (DFG). B. Nestler acknowledges experimental motivation of the research through the programme 'Materials Science and Engineering (MSE)', No. 43.31.01 of the Helmholtz Association. N. Merkert and S. Lyu acknowledge the Deutsche Forschungsgemeinschaft (DFG, German Research Foundation) - Project-ID 394563137 - SFB 1368 for the financial support. H.M. Zhang gratefully acknowledges insightful discussions with Dr. Xiaoying Liu. The authors acknowledge support by the state of Baden-Württemberg through bwHPC.

Supplementary material

Supplementary material associated with this article can be found in the online version at 10.1016/j.jcis.2025.139781.

References

[1] H.-J. Butt, J. Liu, K. Koynov, B. Straub, C. Hinduja, I. Roismann, R. Berger, X. Li, D. Vollmer, W. Steffen, et al., Contact angle hysteresis, Curr. Opin. Colloid Interface Sci. 59 (2022) 101574.
[2] H.-J. Butt, R. Berger, J. De Coninck, R. Tadmor, Drop friction, Nat. Rev. Phys. 7 (8) (2025) 425–438.
[3] A. Marmur, Thermodynamic aspects of contact angle hysteresis, Adv. Colloid Interface Sci. 50 (1994) 121–141.
[4] Extrand, CW, water contact angles and hysteresis of polyamide surfaces, J. Colloid Interface Sci. 248 (1) (2002) 136–142.
[5] Chibowski, Emil, Surface free energy of a solid from contact angle hysteresis, Adv. Colloid Interface Sci. 103 (2) (2003) 149–172.
[6] H. Barrio-Zhang, É. Ruiz-Gutiérrez, S. Armstrong, G. McHale, G.G. Wells, R. Ledesma-Aguilar, Contact-angle hysteresis and contact-line friction on slippery liquid-like surfaces, Langmuir 36 (49) (2020) 15094–15101.
[7] X. Li, F. Bodziony, M. Yin, H. Marschall, R. Berger, H.-J. Butt, Kinetic drop friction, Nat. Commun. 14 (1) (2023) 4571.
[8] H.-J. Butt, R. Berger, W. Steffen, D. Vollmer, S.A.L. Weber, Adaptive wetting-adaptation in wetting, Langmuir 34 (38) (2018) 11292–11304.
[9] X. Li, P. Bista, A.Z. Stetten, H. Bonart, M.T. Schür, S. Hardt, F. Bodziony, H. Marschall, A. Saal, X. Deng, et al., Spontaneous charging affects the motion of sliding drops, Nat. Phys. 18 (6) (2022) 713–719.
[10] A. Uysal, M. Chu, B. Stripe, A. Timalsina, S. Chattopadhyay, C.M. Schlepütz, T.J. Marks, P. Dutta, What x rays can tell us about the interfacial profile of water near hydrophobic surfaces, Phys. Rev. B-Condensed Matter Mater. Phys. 88 (3) (2013) 035431.
[11] S. Chattopadhyay, A. Uysal, B. Stripe, Y.-g. Ha, T.J. Marks, E.A. Karapetrova, P. Dutta, How water meets a very hydrophobic surface, Phys. Rev. Lett. 105 (3) (2010) 037803.
[12] A. Miron, R. Tadmor, V. Multanen, S. Pinkert, Friction of granular systems: the role of solid–liquid interaction, Sci. Rep. 15 (1) (2025) 1–12.
[13] T. Young, III. An essay on the cohesion of fluids, Philosophical Trans. R. Soc. London (95) (1805) 65–87.
[14] F. Wang, B. Nestler, et al., Wetting and contact-angle hysteresis: density asymmetry and van der waals force, Phys. Rev. Lett. 132 (12) (2024) 126202.
[15] H. Zhang, H. Zhang, F. Wang, B. Nestler, Exploration of contact angle hysteresis mechanisms: from microscopic to macroscopic, J. Chem. Phys. 161 (2024) 194705.
[16] F. Wang, H. Zhang, B. Nestler, Wetting phenomena: line tension and gravitational effect, Phys. Rev. Lett. 133 (24) (2024) 246201.
[17] L. Makkonen, A thermodynamic model of contact angle hysteresis, J. Chem. Phys. 147 (6) (2017) 064703.
[18] Z. Zhang, X. Xu, Effective boundary conditions for dynamic contact angle hysteresis on chemically inhomogeneous surfaces, J. Fluid Mech. 935 (2022) A34.
[19] J.C. Fernández-Toledano, T.D. Blake, J. De Coninck, Taking a closer look: a molecular-dynamics investigation of microscopic and apparent dynamic contact angles, J. Colloid Interface Sci. 587 (2021) 311–323.
[20] J.W. Cahn, Critical point wetting, J. Chem. Phys. 66 (8) (1977) 3667–3672.
[21] D. Jacqmin, Contact-line dynamics of a diffuse fluid interface, J. Fluid Mech. 402 (2000) 57–88.
[22] H. Zhang, Y. Wu, F. Wang, B. Nestler, Effect of wall free energy formulation on the wetting phenomenon: conservative Allen–Cahn model, J. Chem. Phys. 159 (2023) 164701.
[23] P. Yue, Thermodynamically consistent phase-field modelling of contact angle hysteresis, J. Fluid Mech. 899 (2020) A15.
[24] J.-J. Huang, H. Huang, X. Wang, Wetting boundary conditions in numerical simulation of binary fluids by using phase-field method: some comparative studies and new development, Int. J. Numer. Methods Fluids 77 (3) (2015) 123–158.
[25] H. Ding, P.D.M. Spelt, Onset of motion of a three-dimensional droplet on a wall in shear flow at moderate Reynolds numbers, J. Fluid Mech. 599 (2008) 341–362.
[26] Y. Chang, S. Wu, Q. Li, B. Pulli, D. Salmi, P. Yock, J.J. Heit, R.R. Zhao, Milli-spinner thrombectomy, Nature 642 (2025) 336–342.
[27] G. Pontrelli, E.J. Carr, A. Tiribocchi, S. Succi, Modeling drug delivery from multiple emulsions, Phys. Rev. E 102 (2) (2020) 023114.
[28] B. Nestler, F. Wendler, M. Selzer, B. Stinner, H. Garcke, Phase-field model for multiphase systems with preserved volume fractions, Phys. Rev. E-Stat. Nonlinear Soft Matter Phys. 78 (1) (2008) 011604.
[29] M. Reder, P.W. Hoffrogge, D. Schneider, B. Nestler, A phase-field based model for coupling two-phase flow with the motion of immersed rigid bodies, Int. J. Numer. Methods Eng. 123 (16) (2022) 3757–3780. https://doi.org/10.1002/nme.6988
[30] M. Reder, A. Prahs, D. Schneider, B. Nestler, Viscous stress approximations in diffuse interface methods for two-phase flow based on mechanical jump conditions, Comput. Methods Appl. Mech. Eng. 432 (2024) 117341. https://doi.org/10.1016/j.cma.2024.117341
[31] E. Ruckenstein, G. Berim, Microscopic description of a drop on a solid surface, Adv. Colloid Interface Sci. 157 (2010) 1–33.
[32] M. Chaudhuri, E. Allahyarov, H. Löwen, S.U. Egelhaaf, D.A. Weitz, Triple junction at the triple point resolved on the individual particle level, Phys. Rev. Lett. 119 (12) (2017) 128001.
[33] P.G. De Gennes, Polymer solutions near an interface. adsorption and depletion layers, Macromolecules 14 (6) (1981) 1637–1644.
[34] H. Zhang, H. Zhang, F. Wang, B. Nestler, Wetting effect induced depletion and adsorption layers: diffuse interface perspective, Chemphyschem 25 (14) (2024) e202400086.
[35] K. Liu, M. Vuckovac, M. Latikka, T. Huhtamäki, R.H.A. Ras, Improving surface-wetting characterization, Science 363 (6432) (2019) 1147–1148.
[36] C. Furmidge, Studies at phase interfaces. I. The sliding of liquid drops on solid surfaces and a theory for spray retention, J. Colloid Sci. 17 (4) (1962) 309–324.
[37] P.D.M. Spelt, A level-set approach for simulations of flows with multiple moving contact lines with hysteresis, J. Comput. Phys. 207 (2) (2005) 389–404.
[38] B.M. Mognetti, H. Kusumaatmaja, J.M. Yeomans, Drop dynamics on hydrophobic and superhydrophobic surfaces, Faraday Discuss. 146 (2010) 153–165.
[39] N. Gao, F. Geyer, D.W. Pilat, S. Wooh, D. Vollmer, H.-J. Butt, R. Berger, How drops start sliding over solid surfaces, Nat. Phys. 14 (2) (2018) 191–196.
[40] L. Gao, T.J. McCarthy, Contact angle hysteresis explained, Langmuir 22 (14) (2006) 6234–6237.
[41] U.M. Mirsaidov, H. Zheng, D. Bhattacharya, Y. Casana, P. Matsudaira, Direct observation of stick-slip movements of water nanodroplets induced by an electron beam, Proc. Natl. Acad. Sci. 109 (19) (2012) 7187–7190.
[42] C.W. Extrand, Y. Kumagai, Liquid drops on an inclined plane: the relation between contact angles, drop shape, and retentive force, J. Colloid Interface Sci. 170 (2) (1995) 515–521.
[43] A. Vinod, Y. Barak, S.Y. Schmid, S. Gulec, Y. Bhimavarapu, A. Jena, D. Katoshevski, N. Haikin, R. Tadmor, Measuring surface energy of solid surfaces using centrifugal adhesion balance, Phys. Rev. E 110 (1) (2024) 014801.
[44] E. Bormashenko, Y. Bormashenko, G. Whyman, R. Pogreb, A. Musin, R. Jager, Z. Barkay, Contact angle hysteresis on polymer substrates established with various experimental techniques, its interpretation, and quantitative characterization, Langmuir 24 (8) (2008) 4020–4025.
[45] C.I. Fisher, S.C. Kuo, Filament rigidity causes F-actin depletion from nonbinding surfaces, Proc. Natl. Acad. Sci. 106 (1) (2009) 133–138.
[46] R. Tadmor, P. Bahadur, A. Leh, H.E. N'guessan, R. Jaini, L. Dang, Measurement of lateral adhesion forces at the interface between a liquid drop and a substrate, Phys. Rev. Lett. 103 (26) (2009) 266101.
[47] H. Zhang, F. Wang, B. Nestler, No-slip, slip and friction at fluid-solid interfaces: concept of adsorption layer, arXiv:2502.18380 (2025).